

SCIENTIFIC REPORTS

OPEN

Room-temperature Magnetism in Carbon Dots and Enhanced Ferromagnetism in Carbon Dots-Polyaniline Nanocomposite

Jian Liu^{1,2}, Hong Bi¹, Paulo Cesar Morais^{1,3}, Xiang Zhang¹, Fapei Zhang⁴ & Lin Hu⁴

Room temperature magnetic ordering is reported for very small carbon dots (CDs), mat-like polyaniline nanofibers (Mat-PANI) and a composite of CDs@Mat-PANI containing 0.315 wt% CDs. We have found saturation magnetization (M_s) of CDs, Mat-PANI and CDs@Mat-PANI at 5 (20/300) K equals to 0.0079 (0.0048/0.0019), 0.0116 (0.0065/0.0055) and 0.0349 (0.0085/0.0077) emu/g, respectively. The M_s enhancement in CDs@Mat-PANI (200% and 40% at 5 K and 300 K, respectively) is attributed to electron transfer from Mat-PANI imine N-atoms to the encapsulated CDs. Changes in M_s values reveal that 0.81 (0.08) electron/CD is transferred at 5 (300) K, which is supported by observation of CDs photoluminescence (PL) redshift while in CDs@Mat-PANI. Band-bending and bandgap-renormalization calculations are used to predict a redshift of 117 meV at 300 K as a result of the electron transfer, in excellent agreement with the PL data (110 meV). Raman, X-ray diffraction and X-ray photoelectron spectroscopy data are used to confirm the electron transfer process as well as the strong interaction of CDs with PANI within CDs@Mat-PANI, which increases the crystalline domain size of Mat-PANI from about 4.8 nm to 9.2 nm while reducing the tensile strain from about 6.2% to 1.8%.

The recent research and technology for new magnetic materials aim to combine room temperature operation, lightweight, low production cost, molding capability and environmental friendliness^{1,2}. Along this line metal-free carbon nanomaterials represent a very promising direction, as for instance in spintronics once carbon may easily integrate spin and molecular electronics into a single platform³⁻⁵. Room-temperature (RT) ferromagnetism in carbon nanomaterials was firstly reported in C₆₀ while synthesized under high-pressure and high-temperature polymerization process^{6,7}. Subsequently, ferromagnetism in different carbon nanomaterials have been reported, e.g. diamonds up to 90 K⁸, carbon nanotubes up to 600 K⁹, and graphene quantum dots (GQDs) at 2 K^{10,11}. As a new member in carbon family, carbon dots (CDs) refer to nanoparticles with size below 10 nm that usually consist of a crystalline core with major sp²-hybridized carbon atoms plus an amorphous shell dominated by different chemical moieties, whose composition ultimately depends upon the carbon source used in the synthesis process^{12,13}. Recently, CDs were extensively explored in regard to their strong photoluminescence (PL) with high quantum yield as well as tunable surface defects and thus optical properties¹⁴⁻¹⁷. In the present study, we pioneering report on RT magnetic ordering in CDs, but also a new metal-free magnetic nanohybrid based on CDs encapsulated within polyaniline (PANI) nanofibers that have been assembled into a three-dimensional (3D) mat-like morphology (Mat-PANI). While RT ferromagnetism was already reported in PANI-based materials^{18,19}, enhancement of ferromagnetism promoted by integrating CDs and Mat-PANI into a single nanohybrid platform labeled as CDs@Mat-PANI is a novelty. In preparation of metal-free samples, much attention was given to the purity of initial reactants and careful synthesis and subsequent procedures in order to prevent samples from being contaminated by metal-based magnetic impurities. This is particularly important while examining weak RT magnetic ordering and its enhancement, as firstly reported here respectively in CDs and CDs@Mat-PANI, and yet not completely understood. Prior to the synthesis of the nanohybrid, CDs were prepared by pyrolysis of konjac

¹College of Chemistry and Chemical Engineering, Anhui University, Hefei, 230601, China. ²Department of Chemical and Chemical Engineering, Hefei Normal University, Hefei, 230601, China. ³Universidade de Brasília, Instituto de Física, Brasília, DF, 70910-900, Brazil. ⁴High Magnetic Field Laboratory of the Chinese Academy Sciences, Hefei, 230031, China. Hong Bi and Paulo Cesar Morais contributed equally to this work. Correspondence and requests for materials should be addressed to H.B. (email: bihong@ahu.edu.cn) or P.C. (email: pcmor@unb.br)

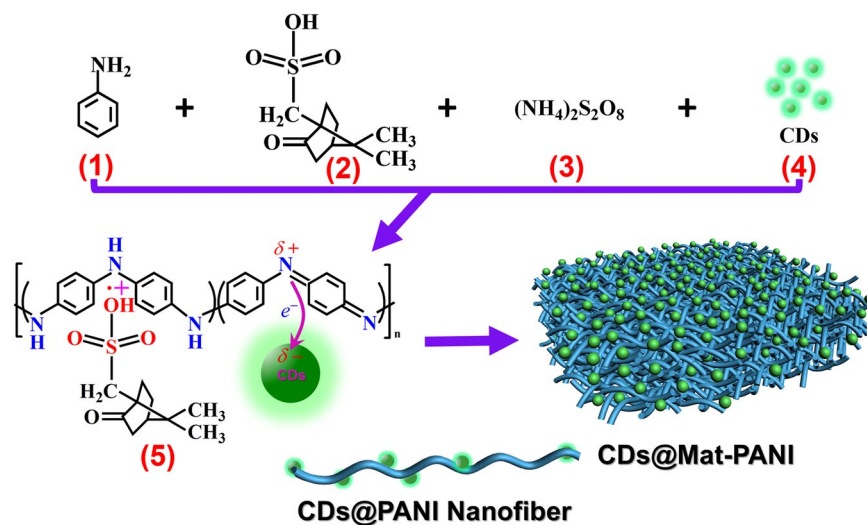


Figure 1. An illustration of the synthesis procedure of CDs@Mat-PANI.

flour (KF, Biosharp Company) and purified repeatedly using ethanol and distilled water according to the protocol described in our previous report²⁰. Elemental analysis of the CDs indicated metal (Fe, Co, Ni, and Mn) trace level below 1 ppm. Figure 1 illustrates the synthesis procedure of CDs@Mat-PANI nanofibers and their entangled 3D mat-like structure. Although PANI with different morphologies had been extensively reported in the literature^{21,22}, mat-like morphology of PANI nanofibers is firstly reported here. We envisaged that the new family of magnetically-ordered CDs and CDs@Mat-PANI will offer multiple opportunities for fundamental studies, due to the modulation of their properties by varying the CDs characteristics, the PANI morphology and their relative content within the nanohybrid, opening up a new avenue for spintronics device fabrication.

Results and Discussion

Figure 2a shows a typical transmission electron microscopy (TEM) image of the quasi-spherical CDs with an average diameter of 2.21 nm. The solid white-line going through the histogram in the inset of Fig. 2a is the best fitting of the data using a lognormal distribution function. Additionally, the inset of Fig. S1a in the Supplementary information shows 0.216 nm lattice fringe of an individual CD, indicating the existence of graphitic crystalline core in the CDs^{12,20}. Figure S1b shows UV-Vis absorbance spectrum of the CDs dispersed in ethanol with an obvious PL emission centred at 331 nm ($\lambda_{em} = 310$ nm). Figure 2b shows a representative scanning electron microscopy (SEM) image of the CDs@Mat-PANI, in which the above-described 3D mat-like morphology with thickness of 2–3 μ m is clearly demonstrated. The corresponding magnified high-resolution TEM (HRTEM) image, as shown in Fig. 2c, confirms the presence of CDs encapsulated within the Mat-PANI nanofibers. The inset of Fig. 2c shows an individual CD in the PANI nanofiber with lattice diffraction fringes of 0.216 nm, which is in excellent agreement with that observed in pure CDs samples (see Fig. S1a). The control sample Mat-PANI shows a similar 3D mat-like morphology (see Fig. S2a,b), but without CDs in the PANI nanofibers (see Fig. S2c), indicating that addition of 0.315 wt% of CDs would not change the mat-like PANI morphology.

Notably, Fig. 1 also illustrates electron transfer from PANI to CDs (see panel 5), which is assumed to occur and plays an important role in defining the very properties of the CDs@Mat-PANI. Figure 3a supports the electron transfer picture from Mat-PANI to CDs, for the RT redshift (from 331 nm to 341 nm) in the PL peak of sample CDs@Mat-PANI is credited to the enhancement of electron density held by the CDs, accompanied with the decrease of electron density in PANI backbone. Figure 3b shows the X-ray diffraction (XRD) data of the as-synthesized samples, where CDs reveal a broad XRD band with a small peak centred at $2\theta = 17.72^\circ$, presenting d-spacing value of 0.413 nm, in good agreement with (002) plane of graphite¹². The Mat-PANI sample exhibits three characteristic XRD peaks of crystalline CSA-doped PANI at $2\theta = 10.00^\circ$, 18.04° and 24.68° , corresponding to d-spacing values of 0.888 nm, 0.497 nm and 0.369 nm for (010), (110) and (200) planes of protonic acid doped PANI, respectively^{23,24}. Besides the three crystalline-PANI-ascribed XRD lines, two other features (2θ) associated to the CDs@Mat-PANI and appearing in Fig. 3b should be explored as well (17.14° and 25.49°). The nanohybrid CDs@Mat-PANI presents clearer and sharper XRD peaks, indicating that its crystallinity has been improved in comparison with Mat-PANI. Analysis of the diffraction peaks in Fig. 3b reveals upshift of the Mat-PANI XRD lines after encapsulation of the CDs, suggesting tensile strain reduction in the nanohybrid²⁵. Assessing five XRD features instead of three planes ((010), (110), and (200)), it is possible to draw the Williamson-Hall plot ($\beta \cos \theta$ versus $\sin \theta$) using the Debye-Scherrer relation corrected for strain, i.e. $\beta \cos \theta = (k\lambda / \langle D \rangle) + 4\epsilon \sin \theta$, where β , θ , k , λ , $\langle D \rangle$ and ϵ are the corrected XRD linewidth, XRD angle, shape constant, XR wavelength, average grain size and strain, respectively²⁶. Needless to mention the shape constant (k) must account for the high aspect ratio value of wire-like morphology of Mat-PANI nanofibers. From the W-H plots shown in Fig. 3c, one can assess the average crystallite grain size ($\langle D \rangle$) and strain (ϵ) equal to 4.8 nm (9.2 nm) and 6.2% (1.8%) for Mat-PANI (CDs@Mat-PANI), respectively. Symbols in Fig. 3c are experimental data (W-H Plot Exp.) whereas solid lines represent the best fittings (W-H Plot Cal.) using the Debye-Scherrer equation mentioned in this paragraph. The ϵ value

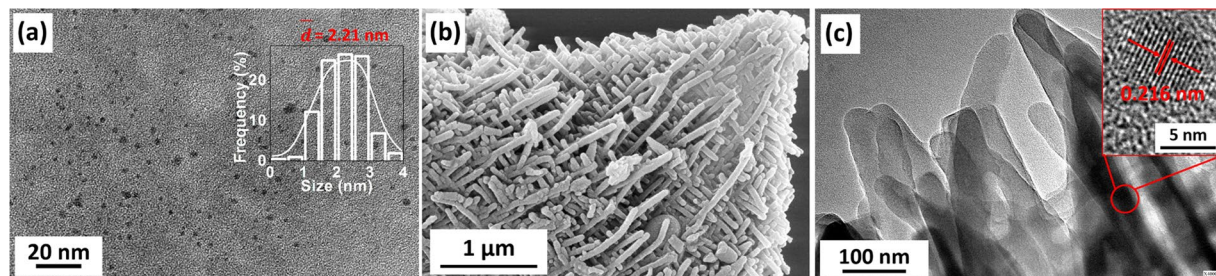


Figure 2. (a) TEM image of CDs (the inset is the particle size histogram of CDs); (b) SEM image of CDs@Mat-PANI; (c) HRTEM image of the brim nanofibers of CDs@Mat-PANI (the inset is a magnified image of an individual CD encapsulated within Mat-PANI nanofiber).

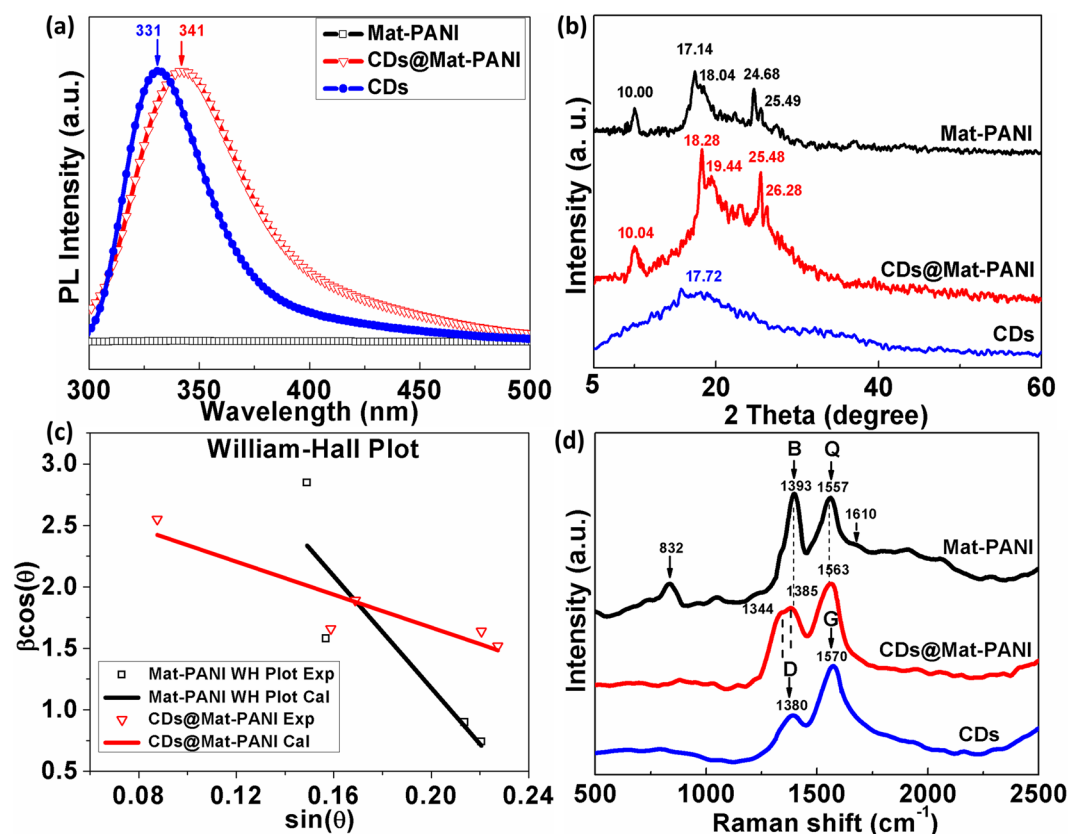


Figure 3. (a) PL spectra, (b) XRD patterns, (c) William-Hall plots of Mat-PANI and CDs@Mat-PANI, and (d) Raman spectra of Mat-PANI, CDs@Mat-PANI, and CDs.

(1.8%) confirms reduction of tensile strain in the nanohybrid while increasing the crystallite average grain size by about 90% with respect to the Mat-PANI sample. This finding will be later on correlated with ferromagnetism enhancement observed in the nanohybrid.

Figure 3d shows two strong Raman features around 1380 and 1570 cm^{-1} in the CDs spectrum, accounting for sp^3 -hybridized (D) and sp^2 -hybridized (G) carbon-carbon vibrations, respectively¹². Differently, Mat-PANI shows a Raman feature around 1557 cm^{-1} , attributed to the C=N stretching vibration in quinomoid ring (Q)^{27,28} whereas Raman features around 1393 and 1610 cm^{-1} had been ascribed to C-N⁺ vibration of delocalized polaronic structures (protonation band PB and B)^{29,30} and C-C stretching of benzenoid ring^{31,32}, respectively. Raman bands appearing in the range of 700–900 cm^{-1} in the Mat-PANI spectrum (particularly 832 cm^{-1} in Fig. 3d) had been attributed to benzene ring or amine deformation in polaronic or bipolaronic forms of PANI²⁷. When comparing Mat-PANI with CDs@Mat-PANI, the Raman spectrum of the latter reveals increased Q-band (1563 cm^{-1}) intensity while reducing B-band (1385 cm^{-1}) intensity, thus supporting the picture of electron transfer from imine Nitrogen atoms of PANI to CDs and then resulting in the decrease of electron density in PANI backbone. Compared with Mat-PANI, the CDs@Mat-PANI sample presents a shift of the C-N⁺ stretching peak towards much lower wavenumbers of 1385 cm^{-1} and 1344 cm^{-1} due to CDs encapsulation into PANI. Previously,

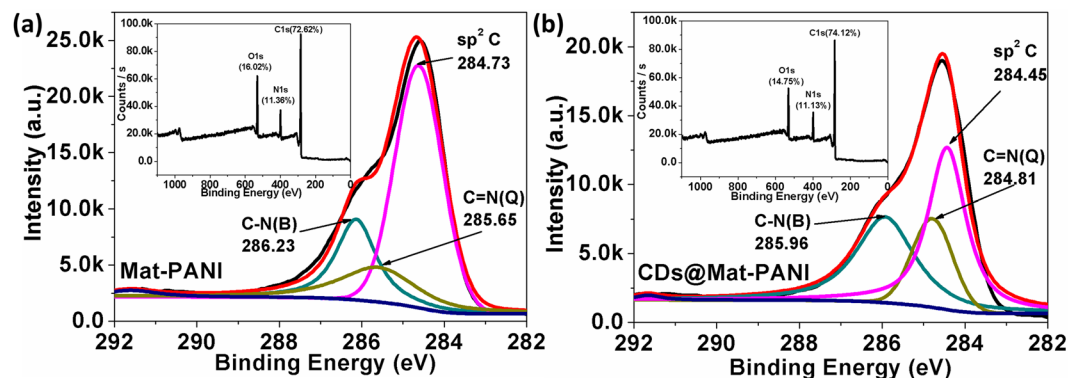


Figure 4. XPS C1s core-level spectra of (a) Mat-PANI and (b) CDs@Mat-PANI. The insets show general XPS spectra of Mat-PANI and CDs@Mat-PANI.

CDs have been reported to exhibit unique photo-induced electron transfer as well as electron acceptor properties³³. Interestingly, the Raman peak at 832 cm^{-1} is completely quenched in the nanohybrid (CDs@Mat-PANI), indicating change in the PANI backbone structure, more likely due to reduction of tensile strain as supported by the XRD peak upshift previously mentioned.

Further, Fig. 4a,b show the X-ray photoelectron spectroscopy (XPS) C1s core-level spectra of Mat-PANI and CDs@Mat-PANI, supporting the electron transfer process from Mat-PANI to CDs. The Gaussian fitted C1s binding energies of Mat-PANI at 284.73, 285.65 and 286.23 eV (see Fig. 4a) can be attributed to sp^2C of benzenoid ring, C=N stretching vibration in quinoid structure (labeled as C=N(Q)) and C-N^+ delocalized polaronic structures (labeled as C-N(B)), respectively^{34,35}. Similarly, the C1s core level spectrum of CDs@Mat-PANI can be resolved into three Gaussian peaks at 284.45, 284.81 and 285.96 eV (see Fig. 4b), corresponding to sp^2C , C=N(Q) and C-N(B) species, respectively. Note that the binding energies of sp^2C , C=N and C-N^+ species in CDs@Mat-PANI are all downshifted with respect to Mat-PANI, which can be ascribed to electron transfer from PANI to CDs in the nanohybrid, in good agreement with the Raman data shown in Fig. 3d. The insets of Fig. 4a,b show the general XPS spectra of Mat-PANI and CDs@Mat-PANI.

Figure 5 shows the magnetization data of the as-synthesized samples at 5, 20 and 300 K ($\pm 30\text{ kOe}$ range), whereas the saturation magnetization (M_s) and magnetic coercivity (H_c) of Mat-PANI, CDs@Mat-PANI and CDs are collected in Table 1. Figure 5a(i), b(i) and c(i) show the hysteresis cycles in the $\pm 0.12\text{ kOe}$ range, revealing magnetic ordering of samples CDs, Mat-PANI and CDs@Mat-PANI at 5, 20 and 300 K, respectively. Figure 5a(ii), b(ii) and c(ii) show the hysteresis cycles after removing the diamagnetic component. In addition to the novelty of RT magnetic ordering of CDs, the CDs@Mat-PANI sample shows enormous enhancement of M_s (about 200% (40%) at 5 (300) K) with respect to Mat-PANI (see data in Table 1). Neglecting any interaction between the two constituent phases (CDs and Mat-PANI), the expected M_s of the nanohybrid (CDs@Mat-PANI) at 5 K would be around 0.0116 emu/g (Vegard's law), given the nominal CDs content of 0.315 wt%. However, the measured M_s of the nanohybrid is three-fold larger (0.0349 emu/g), revealing that there is indeed a strong interaction between CDs and Mat-PANI in the CDs@Mat-PANI.

Magnetic ordering in metal-free carbon nanomaterials has been attributed to the coupling of unpaired electrons^{36,37} and supported by *ab initio* calculation^{38–40}. Therefore, in CDs magnetic ordering is realized in the framework of coupling of unpaired electrons, likely associated with the shell layer, while ascribing to the CDs core region the quantum confined semiconductor nature. In contrast with GQDs, where ferromagnetism has been reported only at very low temperature^{10,11} (2 K), an extra exchange interaction term, besides the usual spin-spin one ($J_{ij}S_i \cdot S_j$), may account for RT magnetic ordering in CDs. The extra Hamiltonian term should describe a non-flat array of spins in CDs, as opposed to the flat array of spin centers in GQDs. On the other hand, ferromagnetism in PANI-related structures has been connected to the existence of two spin species associated with metallic islands (ordered crystalline region) immersed in low conducting matrix (amorphous regions)^{41,42}. The existence of crystalline and amorphous regions within PANI has been generally accepted and clear experimental evidences of it had been provided in the work of Beau *et al.*⁴³. Furthermore, it has been shown that magnetic ordering in PANI-related materials increased while increasing the crystallinity degree of the polymer⁴⁴.

Our findings regarding the enhancement of magnetic ordering in the nanohybrid sample fit nicely with the electron transfer model picture drawn to explain the observed PL redshift of the CDs while encapsulated into the Mat-PANI. As the electron density within the CDs increases the optical energy transition shrinks in due to shift of energy levels in the CDs. Worth mentioning that the CDs incorporated within PANI were slightly negatively charged, as assessed from zeta-potential measurements. Band-bending plus bandgap renormalization accounted for the reduction ($-\Delta E$) of the effective bandgap of the CDs, namely $-\Delta E = \rho + 4.27\rho^{1/3}$, where ΔE is expressed in meV and ρ (charge density) in units of 10^{18} cm^{-3} ^{45,46}. In the above equation for ΔE the linear term (ρ) describes band-bending whereas the non-linear term ($4.27\rho^{1/3}$) describes bandgap renormalization⁴⁵. From the analysis of the M_s data at 300 K (5 K) of Mat-PANI, CDs@Mat-PANI and CDs, we found that in average 0.08 (0.81) electron was transferred from the Mat-PANI backbone (imine N-atoms) to each CD (see next paragraph). At 300 K this means an increase in electron density within each CD of about $\Delta\rho = 14.2 \times 10^{18}\text{ cm}^{-3}$. The estimated value of $\Delta\rho$ can be used in the above equation for $-\Delta E$ to obtain the energy shift of about 117 meV. On the other

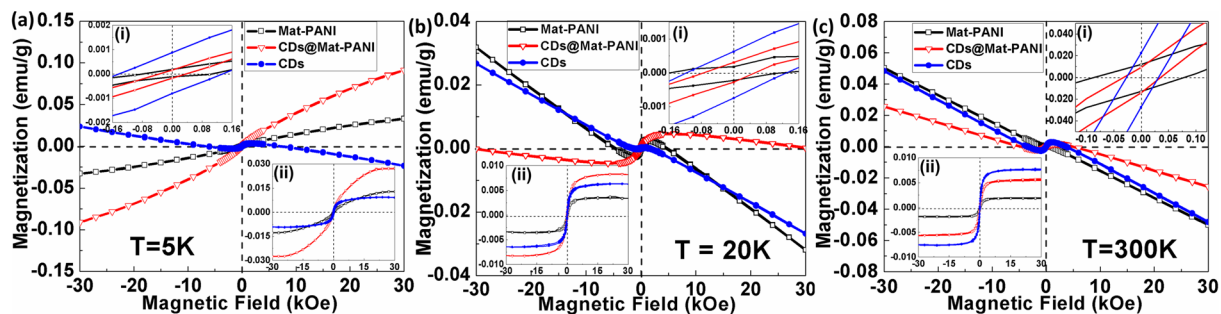


Figure 5. Magnetic hysteresis curves of the Mat-PANI, CDs@Mat-PANI and CDs at (a) 5 K, (b) 20 K, and (c) 300 K. The insets of (a(i)), (b(i)) and (c(i)) show magnetic hysteresis curves of Mat-PANI, CDs@Mat-PANI and CDs in the range of ± 0.12 kOe. The insets of (a(ii)), (b(ii)) and (c(ii)) show the hysteresis curves after subtracting the diamagnetic component.

T (K)	Mat-PANI		CDs@Mat-PANI		CDs	
	M_S (emu/g)	H_C (kOe)	M_S (emu/g)	H_C (kOe)	M_S (emu/g)	H_C (kOe)
300	0.0055	0.04	0.0077	0.03	0.0019	0.09
20	0.0065	0.12	0.0085	0.07	0.0048	0.16
5	0.0116	0.08	0.0349	0.04	0.0079	0.14

Table 1. Saturation magnetization (M_S) and magnetic coercivity (H_C) of Mat-PANI, CDs@Mat-PANI and CDs at 300, 20 and 5 K.

hand, at 300 K we found the redshift of the PL line equals to 110 meV (Fig. 3a). Deviation of only 7 meV from the calculated value to the experimental PL redshift is indeed an excellent result, given the difference between the two approaches, i.e. magnetization data used to extract $\Delta\rho$ versus optical data to assess PL shift (calculation has been shown in Supplementary information).

We can elaborate further the magnetic ordering enhancement in the nanohybrid as due to increase of density of unpaired electrons (spin-1/2 sites) within the Mat-PANI backbone via transferring electrons out from imine Nitrogen atoms into neighboring CDs, with consequent increase of electron density within the latter. The enhancement in M_S of the nanohybrid at 300 K (5 K) is about 0.0022 emu/g (0.0233 emu/g), meaning an increase of about $2.3723 \times 10^{17} \mu_B/g$ ($2.5124 \times 10^{18} \mu_B/g$). This implies that in average about 0.08 (0.81) electron is transferred to each CD at 300 K (5 K), thus increasing the number of unpaired electrons in the Mat-PANI backbone surrounding the CDs by the same amount. Given the spherical shape of the CDs with average diameter of about 2.21 nm (see Fig. 2a), the negative charge density transferred to each dot ($\Delta\rho$) at 300 K amounts $14.2 \times 10^{18} \text{ cm}^{-3}$. Additionally, improved crystallinity in the CDs@Mat-PANI accounted for the increase of crystalline domain size from about 4.8 nm in Mat-PANI to 9.2 nm in CDs@Mat-PANI, with the corresponding reduction of tensile strain from about 6.2 to 1.8%, which supports the picture that the observed magnetic ordering enhancement is mainly due to electron density changes in the Mat-PANI triggered by strong interaction with CDs.

In summary, we reported room-temperature magnetic ordering in very small CDs and enhancement of ferromagnetism in CDs-incorporated mat-like PANI with a very low incorporation content of 0.315 wt%. The strong interaction between PANI and CDs occurred in a way of electron transfer from Mat-PANI imine N-atoms to the neighbouring CDs. The electron transfer process was confirmed by Raman, XRD and XPS data as well as PL redshift result, which increased electron density in the CDs while reduced the electron density in the PANI backbone. As a result, the increased number of unpaired electrons in the PANI backbone enhanced remarkably the M_S value of the nanohybrid (CDs@Mat-PANI).

Methods

Synthesis. In a typical synthesis process of CDs@Mat-PANI 2.23 g of aniline monomer (Shanghai Chemical Company) distilled under reduced pressure, 0.93 g of camphorsulfonic acid (CSA, Aladdin Industrial Corporation) and 10 mg of CDs (see panels (1), (2) and (4) in Fig. 1) were dispersed in 500 mL deionized water under magnetic stirring at 20–30 °C for 10 min. Next, the mixture was maintained at 30 °C in water bath for 1 h and then 500 mL aqueous solution containing 5.47 g of ammonium persulfate (APS, Sinopharm Chemical Reagent Company) was added to the above mixture in one portion (see panel (3) in Fig. 1). The resulting solution was stirred for a while to ensure complete mixing and then the reaction was allowed to proceed without agitation at 30 °C for 20 h. Finally, the yielded product was washed with deionized water and ethanol repeatedly until filtrate became colourless and then dried under vacuum at 80 °C for 24 h to obtain the dark-blue CDs@Mat-PANI sample. As a control, Mat-PANI sample was prepared by a similar *in-situ* polymerization procedure of the same amounts of aniline and CSA initiated by APS in deionized water.

Characterization. Samples morphologies were observed by using scanning electron microscopy (Hitachi S-4800) and transmission electron microscopy (Hitachi H-800). The X-ray diffraction powder patterns were collected using a Rigaku D/MAX-cA X-ray diffractometer equipped with Cu K α radiation ($\lambda = 1.5406 \text{ \AA}$) over the 2θ range of 5–60 degree. X-ray photoelectron spectroscopy studies were carried out on an ESCALAB250 spectrophotometer. Raman and photoluminescence spectra were obtained using a LabRAM HR800 Raman spectroscopy and an UV532 spectrophotometer, respectively. Magnetic hysteresis curves were recorded with a SQUID magnetic measuring system (Quantum Design MPMS) in magnetic fields up to 30 kG at 5, 20, and 300 K.

References

- Kuemmeth, F., Ilani, S., Ralph, D. C. & McEuen, P. L. Coupling of spin and orbital motion of electrons in carbon nanotubes. *Nature* **452**, 448–452, doi:10.1038/nature06822 (2008).
- Magda, G. Z. *et al.* Room-temperature magnetic order on zigzag edges of narrow graphene nanoribbons. *Nature* **514**, 608–611, doi:10.1038/nature13831 (2014).
- Xia, H. H. *et al.* Tunable magnetism in carbon-ion-implanted highly oriented pyrolytic graphite. *Adv. Mater.* **20**, 4679–4683, doi:10.1002/adma.200801205 (2008).
- Pesin, D. & MacDonald, A. H. Spintronics and pseudospintronics in graphene and topological insulators. *Nature Mater.* **11**, 409–416, doi:10.1038/nmat3305 (2012).
- Awschalom, D. D., Bassett, L. C., Dzurak, A. S., Hu, E. L. & Petta, J. R. Quantum spintronics: engineering and manipulating atom-like spins in semiconductors. *Science* **339**, 1174–1179, doi:10.1126/science.1231364 (2013).
- Wood, R. A. *et al.* Ferromagnetic fullerene. *J. Phys. Condens. Mat.* **14**, 385–391, <http://iopscience.iop.org/0953-8984/14/22/101> (2002).
- Esquinazi, P. *et al.* Induced magnetic ordering by proton irradiation in graphite. *Phys. Rev. Lett.* **91**, 227201, doi:10.1103/PhysRevLett.91.227201 (2003).
- Talapatra, S. *et al.* Irradiation-induced magnetism in carbon nanostructures. *Phys. Rev. Lett.* **95**, 097201, doi:10.1103/PhysRevLett.95.097201 (2005).
- Friedman, A. L. *et al.* Possible room-temperature ferromagnetism in hydrogenated carbon nanotubes. *Phys. Rev. B* **81**, 115461, doi:10.1103/PhysRevB.81.115461 (2010).
- Cervenka, J., Katsnelson, M. I. & Flipse, C. F. J. Room-temperature ferromagnetism in graphite driven by two-dimensional networks of point defects. *Nat. Phys.* **5**, 840–844, doi:10.1038/nphys1399 (2009).
- Swain, A. K. & Bahadur, D. Deconvolution of mixed magnetism in multilayer grapheme. *Appl. Phys. Lett.* **104**, 242413, doi:10.1063/1.4884426 (2014).
- Li, H. T., Kang, Z. H., Liu, Y. & Lee, S. T. Carbon nanodots: synthesis, properties and applications. *J. Mater. Chem.* **22**, 24230, doi:10.1039/c2jm34690g (2012).
- Lim, S. Y., Shen, W. & Gao, Z. Q. Carbon quantum dots and their applications. *Chem. Soc. Rev.* **44**, 362–381, doi:10.1039/c4cs00269e (2015).
- Cao, L. *et al.* Carbon dots for multiphoton bioimaging. *J. Am. Chem. Soc.* **129**, 11318–11319, doi:10.1021/ja0735271 (2007).
- Baker, S. N. & Baker, G. A. Luminescent carbon nanodots: emergent nanolights. *Angew. Chem. Int. Ed.* **49**, 6726–6744, doi:10.1002/anie.200906623 (2010).
- Dong, Y. Q. *et al.* Natural carbon-based dots from humic substances. *Sci. Rep.* **5**, 10037, doi:10.1038/srep10037 (2015).
- Kang, S. H. *et al.* Ultrafast method for selective design of graphene quantum dots with highly efficient blue emission. *Sci. Rep.* **6**, 38423, doi:10.1038/srep38423 (2016).
- Long, Y. Z. *et al.* Magnetic properties of conducting polymer nanostructures. *J. Phys. Chem. B* **110**, 23228–23233, doi:10.1021/jp062262e (2006).
- Long, Y. Z. *et al.* Recent advances in synthesis, physical properties and applications of conducting polymer nanotubes and nanofibers. *Prog. Polym. Sci.* **36**, 1415–1442, doi:10.1016/j.progpolymsci.2011.04.001 (2011).
- Teng, X. Y. *et al.* Green synthesis of nitrogen-doped carbon dots from konjac flour with “off-on” fluorescence by Fe³⁺ and L-lysine for bioimaging. *J. Mater. Chem. B* **2**, 4631–4639, doi:10.1039/c4tb00368c (2014).
- Stejskal, J., Sapurina, I. & Trchová, M. Polyaniline nanostructures and the role of aniline oligomers in their formation. *Prog. Polym. Sci.* **35**, 1420–1481, doi:10.1016/j.progpolymsci.2010.07.006 (2010).
- Tran, H. D. *et al.* The oxidation of aniline to produce “polyaniline”: a process yielding many different nanoscale structures. *J. Mater. Chem.* **21**, 3534–3550, doi:10.1039/C0JM02699A (2011).
- Pouget, J. P., Jdzefowicz, M. E., Epstein, A. J., Tang, X. & MacDiarmid, A. G. X-ray structure of polyaniline. *Macromolecules* **24**, 779–789, doi:10.1016/0379-6779(91)91170-F (1991).
- Kwon, W., Do, S., Kim, J. H., Jeong, M. S. & Rhee, S. W. Control of photoluminescence of carbon nanodots via surface functionalization using parasubstituted anilines. *Sci. Rep.* **5**, 12604, doi:10.1038/srep12604 (2015).
- FreitasNeto, E. S. *et al.* Temperature-dependent Raman study of thermal parameters in CdS quantum dots. *Nanotechnology* **23**, 125701, doi:10.1088/0957-4484/23/12/125701 (2012).
- Waseda, Y., Matsubara, E. & Shinoda, K. *X-ray diffraction crystallography* (Springer, 2011).
- Cochet, M. *et al.* Theoretical and experimental vibrational study of polyaniline in base forms: non-planar analysis. Part I. *J. Raman Spectrosc.* **31**, 1029–1039, doi:10.1002/1097-4555(200011)31:11<1029::AIDJRS640>3.0.CO;2-A (2000).
- Puthirath, A. B., Raman, S. M., Varma, S. J. & Jayalekshmi, S. Exceptionally crystalline and conducting acid doped polyaniline films by level surface assisted solution casting approach. *Appl. Phys. Lett.* **108**, 161901, doi:10.1063/1.4947083 (2016).
- Mazeikiene, R., Niaura, G. & Malinauskas, A. *In situ* Raman spectroelectrochemical study of electrocatalytic processes at polyaniline modified electrodes: Redox vs. metal-like catalysis. *Electrochem. Commun.* **7**, 1021–1026, doi:10.1016/j.elecom.2005.06.010 (2005).
- Yan, J. *et al.* Preparation of a graphene nanosheet/polyaniline composite with high specific capacitance. *Carbon* **48**, 487–493, doi:10.1016/j.carbon.2009.09.066 (2010).
- Quillard, S., Louarn, G., Lefrant, S. & MacDiarmid, A. G. Vibrational analysis of polyaniline: A comparative study of leucoemeraldine, emeraldine, and pernigraniline bases. *Phys. Rev. B* **50**, 12496–12508, doi:10.1103/PhysRevB.50.12496 (1994).
- Wei, Z. X., Wan, M. X., Lin, T. & Dai, L. M. Polyaniline nanotubes doped with sulfonated carbon nanotubes made via a self-assembly process. *Adv. Mater.* **15**, 136–139, doi:10.1002/adma.200390027 (2003).
- Wang, X. *et al.* Photoinduced electron transfers with carbon dots. *Chem. Commun.* **25**, 3774–3776, doi:10.1039/b906252a (2009).
- Pei, Z. X. *et al.* Synergistic effect in polyaniline-hybrid defective ZnO with enhanced photocatalytic activity and stability. *J. Phys. Chem. C* **118**, 9570–9577, doi:10.1021/jp5020143 (2014).
- Kang, E. T., Neoh, K. G. & Tan, K. L. Polyaniline: A polymer with many interesting intrinsic redox states. *Prog. Polym. Sci.* **23**, 277–324, doi:10.1016/S0079-6700(97)00030-0 (1998).
- Banhart, F., Kotakoski, J. & Krasheninnikov, A. V. Structural defects in graphene. *ACS Nano* **5**, 26–41, doi:10.1021/nn102598m (2011).

37. Kompan, M. E., Sapurina, I. Y., Babayan, V. & Kazantseva, N. E. Electrically conductive polyaniline—A molecular magnet with the possibility of chemically controlling the magnetic properties. *Phys. Solid State* **54**, 2400–2406, doi:10.1134/S1063783412120190 (2012).
38. Andriotis, A. N., Menon, M., Sheetz, R. M. & Chernozatonskii, L. Magnetic properties of C₆₀ polymers. *Phys. Rev. Lett.* **90**, 026801, doi:10.1103/PhysRevLett.90.026801 (2003).
39. Lehtinen, P. O., Foster, A. S., Ma, Y. C., Krasheninnikov, A. V. & Nieminen, R. M. Irradiation-induced magnetism in graphite: A density functional study. *Phys. Rev. Lett.* **93**, 187202, doi:10.1103/PhysRevLett.93.187202 (2004).
40. Zanolli, Z. & Charlier, J. C. Spin transport in carbon nanotubes with magnetic vacancy-defects. *Phys. Rev. B* **81**, 165406, doi:10.1103/PhysRevB.81.165406 (2010).
41. Ginder, J. M., Richter, A. F., MacDiarmid, A. G. & Epstein, A. J. Insulator-to-metal transition in polyaniline. *Solid State Commun.* **63**, 97–101, doi:10.1016/0379-6779(87)90896-4 (1987).
42. Sariciftci, N. S., Heeger, A. J. & Cao, Y. Paramagnetic susceptibility of highly conducting polyaniline: Disordered metal with weak electron-electron interactions (Fermi glass). *Phys. Rev. B* **49**, 5988–5992, doi:10.1103/PhysRevB.49.5988 (1994).
43. Beau, B., Travers, J. P. & Banka, E. NMR evidence for heterogeneous disorder and quasi-1D metallic state in polyaniline CSA. *Synth. Met* **101**, 772–775, doi:10.1016/S0379-6779(98)00357-9 (1999).
44. Zaidi, N. A., Giblin, S. R., Terry, I. & Monkman, A. P. Room temperature magnetic order in an organic magnet derived from polyaniline. *Polymer* **45**, 5683–5689, doi:10.1016/j.polymer.2004.06.002 (2004).
45. Cardoso, A. J. C., Morais, P. C. & Cox, H. M. Investigation of many-body effects in one-side modulation-doped InP-InGaAs heterostructure. *Appl. Phys. Lett.* **68**, 1105–1107, doi:10.1063/1.115727 (1996).
46. Aleksandrov, I. & Zhuravlev, K. Photoluminescence of GaN/AlN quantum dots at high excitation powers. *Phys. Status Solidi C* **7**, 2230–2232, doi:10.1002/pssc.200983469 (2010).

Acknowledgements

This work was financed by the National Natural Science Foundations of China (Grant no. 51272002), the University Science Research Project of Anhui Province (No. KJ2016A577) and the Imported Talent Team Project of Anhui Provincial Department of Education (2015[211]). All of the co-authors thank the Key Laboratory of Environment-Friendly Polymer Materials of Anhui Province and the Key Laboratory of Opto-electronic Information Acquisition and Manipulation, Ministry of Education, Anhui University.

Author Contributions

H.B. planned the experiments. H.B. and P.C.M. wrote the manuscript and analyzed the experimental data. J.L. contributed to the experimental planning and recorded the S.E.M., T.E.M., P.L., X.P.S. and Raman data. Z.X. contributed to the T.E.M. measurements. F.P.Z. and L.H. contributed to the M-H measurements. All authors contributed in the discussion of the results.

Additional Information

Supplementary information accompanies this paper at doi:10.1038/s41598-017-01350-x

Competing Interests: The authors declare that they have no competing interests.

Publisher's note: Springer Nature remains neutral with regard to jurisdictional claims in published maps and institutional affiliations.



Open Access This article is licensed under a Creative Commons Attribution 4.0 International License, which permits use, sharing, adaptation, distribution and reproduction in any medium or format, as long as you give appropriate credit to the original author(s) and the source, provide a link to the Creative Commons license, and indicate if changes were made. The images or other third party material in this article are included in the article's Creative Commons license, unless indicated otherwise in a credit line to the material. If material is not included in the article's Creative Commons license and your intended use is not permitted by statutory regulation or exceeds the permitted use, you will need to obtain permission directly from the copyright holder. To view a copy of this license, visit <http://creativecommons.org/licenses/by/4.0/>.

© The Author(s) 2017